Scalable Multi-Core Dual-Polarization Coherent Receiver Using a Metasurface Optical Hybrid

Kento Komatsu , Go Soma , Shota Ishimura , Hidenori Takahashi , *Member, IEEE*,
Takehiro Tsuritani , *Member, IEEE*, Masatoshi Suzuki , *Life Fellow, IEEE*, Yoshiaki Nakano , *Fellow, IEEE*,
and Takuo Tanemura , *Member, IEEE*

(Post-Deadline Paper)

Abstract—The space-division multiplexed (SDM) coherent transmission using a multi-core fiber (MCF) is a promising technology for further increasing the capacity of optical communications and interconnects. For broader application of SDM systems, dual-polarization (DP) coherent receivers that can be directly coupled to MCFs without bulky fan-in/fan-out (FIFO) devices and polarization beam splitters (PBSs) are desirable. Unlike intensity-modulation direct-detection (IMDD) receivers, however, scaling a DP coherent receiver to multiple spatial channels in a compact form factor is not straightforward. Here, we propose and demonstrate a compact and scalable surface-normal multi-core DP coherent receiver using an ultrathin dielectric metasurface (MS). The MS is composed of silicon nanoposts on quartz, which are judiciously designed to function as the DP optical hybrids and focusing lenses for all spatial channels. Using the fabricated device, simultaneous homodyne detection of DP 64-ary quadrature-amplitude-modulation signals from a four-core fiber is demonstrated with an error vector magnitude of less than 3% for all spatial/polarization channels from 1530 to 1570 nm. The demonstrated receiver can be assembled into a compact module to enable low-cost SDM coherent receivers without bulky PBS and FIFO devices.

Index Terms—Coherent receiver, optical hybrid, multi-core fiber, metasurface.

I. INTRODUCTION

OVER the past few decades, numerous key technologies have been introduced in optical communications to address the continuously growing data traffic [1], [2]. In the 2010 s, dual-polarization (DP) digital coherent systems were put into practical use, which have substantially expanded the transmission capacity by fully utilizing optical phase and polarization degrees of freedom, in addition to optical intensity employed in intensity-modulation and direct-detection (IMDD) systems. Digital coherent systems, which have initially become dominant in the backbone and metro networks, are now expanding to shorter-reach networks, such as datacenter interconnects and optical access [3], [4], [5].

Another emerging technology to expand the transmission capacity is the space-division multiplexing (SDM) that utilizes multiple spatial modes of a multi-core fiber (MCF) or a multi-mode fiber (MMF) as an additional transmission degree of freedom [6], [7], [8]. In particular, use of uncoupled MCFs is expected in the near-future practical systems since they do not require power-hungry multi-input multi-output (MIMO) processing to compensate for complex modal coupling among spatial channels [9], [10]. SDM systems using dual-core uncoupled MCF have recently been deployed in submarine links, which will be in service in a few years [11]. We can expect that such SDM systems would extend to shorter-reach networks, where compact and cost-effective multi-core DP coherent transceivers would be desired.

In order to handle multi-core DP coherent signals in a scalable manner, integrated transceivers that can be coupled directly to MCFs without bulky fan-in/fan-out (FIFO) devices and polarization beam splitters (PBSs) would be ideal. For IMDD systems, multi-core integrated transceivers using vertical-cavity surface-emitting lasers and surface-illuminating photodetector (PD) arrays have been demonstrated [12]. Unlike IMDD format, however, dense 2D array of coherent receivers are challenging to realize due to their inherent complexity. As a result, a coherent receiver that can directly receive multi-core DP coherent signals from an MCF has never been demonstrated to our knowledge.

A straightforward approach to scale conventional integrated waveguide-based receivers to multiple 2D spatial channels is to use arrayed grating couplers (GCs). Indeed, single-polarization
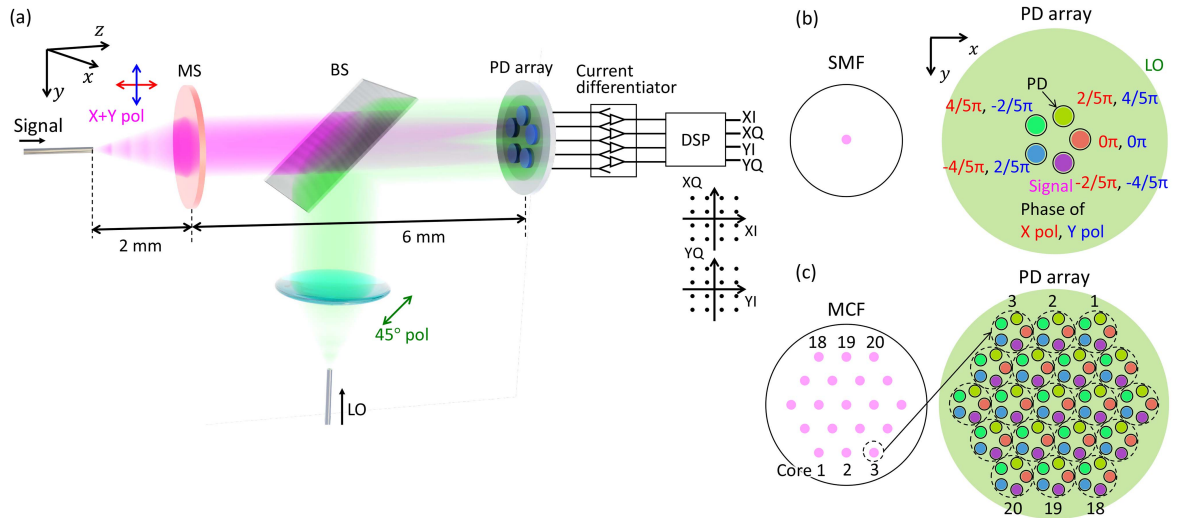
Fig. 1. Proposed spatially scalable DP coherent receiver. (a) Schematic of the receiver when a single signal is input from an SMF. (b) Spatial distributions of signal and LO lightwaves on the PD array plane (a) when a single signal is input from an SMF and (c) when multiple signals are input from a 19-core MCF. In both configurations, the same MS can be used.

signals from an MCF can be efficiently coupled to multiple single-mode waveguides using fan-shaped GCs [13], [14], [15]. In a DP coherent receiver, however, both polarization signals need to be coupled to multiple waveguides simultaneously, which makes use of GCs challenging. A polarization-separating (PS) GC that guides x- and y-polarization components to separate waveguides in different directions has been explored [16], [17], [18]. However, PSGCs generally require a large footprint and/or complicated routing to two independent waveguides per each PSGS, which make these devices not easily scalable to a dense 2D coherent receiver array. To this end, we have recently proposed an alternative approach of realizing a scalable multi-core DP coherent receiver using a dielectric metasurface (MS) and a high-speed PD array [19]. The MS consists of an array of silicon (Si) nanoposts, which were designed judiciously to focus signal light from each core to five PDs with precisely controlled polarization-dependent phases. By mixing with a local oscillator (LO) light, IQ signals of both polarizations were retrieved from five photocurrent signals without using FIFO or PBS. The designed MS was fabricated on a compact silicon-on-quartz (SOQ) chip to demonstrate simultaneous demodulation of four DP coherent signals from a four-core step-index MCF at 1550-nm wavelength.

In this article, we provide a rigorous analysis of the receiver sensitivity of the proposed receiver and derive an explicit condition for the MS to achieve the highest sensitivity. Furthermore, detailed design methodology of MS, comprehensive experimental results using an SMF, and additional experimental investigations on broad wavelength operation from 1530 to 1570 nm are provided.

Throughout this paper, we employ following mathematical notations: $\langle c(t) \rangle$ denotes the expected value of a scalar function $c(t)$, $\|\boldsymbol{v}\|$ is the Euclidean norm of a vector $\boldsymbol{v}$, $\mathbf{M}^{\mathrm{T}}$, $\mathbf{M}^{\dagger}$, $\|\mathbf{M}\|_F$, and $\mathrm{tr}(\mathbf{M})$ are the transpose matrix, the adjoint matrix, the Frobenius norm, and the trace of a matrix $\mathbf{M}$, respectively.

II. DEVICE CONCEPT

The configuration of the proposed SDM DP coherent receiver is shown in Fig. 1. Fig. 1(a) illustrates the case where a single-channel DP coherent signal is coupled from an SMF [20]. Signal light emitted from an SMF is incident on the MS and is focused with equal intensity at five points forming a regular pentagon on the surface of a PD array. Optical phases at respective focal points are designed to maximize the detection sensitivity as we will discuss in the next subsection. In an optimal case, the phases of adjacent focusing points differ by $2\pi/5$ and $4\pi/5$ for x and y polarizations, respectively, as shown in Fig. 1(b). Then, collimated LO light with $45°$ linear polarization is combined and irradiated onto the same PD array, so that signal-LO beat components are detected. The nonlinear signal-signal beat noise can be eliminated effectively by taking the difference between the photocurrents of adjacent PDs. Subsequently, we obtain four real-valued electrical signals, from which the four distinct elements of DP coherent signal (i.e., in-phase and quadrature signals of both polarization components) can be retrieved through 4×4 linear operation by digital signal processing (DSP).

We should note that this device relies on the same principle as the waveguide-based coherent receiver with five PDs, demonstrated by the authors [21]. Compared with conventional DP coherent receivers, which require eight PDs (or four balanced PDs) [22], [23], [24], the number of PDs in our receiver is reduced to five. As a result, we can minimize the footprint of the PD array. Moreover, owing to its surface-normal configuration, the proposed scheme can naturally be scaled to receive spatially parallelized coherent signals. Since the MS acts as a focusing lens, multiple signal beams from different input positions are focused to five points at shifted positions. This feature enables simultaneous detection of multiple signals from all cores when an MCF is placed at the input as shown in Fig. 1(c). Importantly, this can be accomplished without modifying the MS or other optical

components. Consequently, this configuration offers inherent scalability with respect to the number of channels, enabling compact implementation of SDM digital coherent receivers.

A. Theory

Here, we present an analytical model of a generalized surface-normal DP coherent receiver comprising N PDs. To describe the electric field distributions of the x- and y-polarization components on the PD array surface for the signal and LO lightwaves, respectively, we use Jones vectors denoted as

$$\boldsymbol{E}_{\text{sig}} = \begin{bmatrix} a_1(x,y)A_1(t) \\ a_2(x,y)A_2(t) \end{bmatrix}, \quad \boldsymbol{E}_{\text{LO}} = \begin{bmatrix} b_1(x,y) \\ b_2(x,y) \end{bmatrix}, \quad (1)$$

where $(A_1(t), A_2(t))$ ($|A_1|^2, |A_2|^2 \leq 1$) represent the normalized complex IQ amplitudes for both polarizations. Since the electric field at the PD array surface is described as $\boldsymbol{E}(t) = (\boldsymbol{E}_{\text{sig}} + \boldsymbol{E}_{\text{LO}})e^{i\omega_c t}$, where ω_c is the carrier angular frequency, the photocurrent I_n ($n = 1, \ldots, N$) of n-th PD is described as

$$I_n = \frac{R}{2} \iint_{\text{PD}_n} \|\boldsymbol{E}\|^2 dxdy$$
$$= \frac{R}{2}P_{bn} + \frac{R}{2}(P_{a1n}|A_1|^2 + P_{a2n}|A_2|^2) + RQ_n\boldsymbol{A}, \quad (2)$$

where R is the responsivity of PD. The first term, P_{bn}, denotes the LO-LO beat component, which is spatially integrated within the entire detection area of n-th PD and is written as

$$P_{bn} \equiv \iint_{\text{PD}_n} (|b_1|^2 + |b_2|^2)dxdy. \quad (3)$$

Similarly, P_{a1n} and P_{a2n} in the second term in (2) represent the signal-signal beat components for the x and y polarizations, respectively, and are defined as

$$P_{akn} \equiv \iint_{\text{PD}_n} |a_k|^2 dxdy \quad (k = 1, 2). \quad (4)$$

Finally, the third term in (2) represents the signal-LO beat component using $\boldsymbol{Q}_n$ and $\boldsymbol{A}$, which are defined as

$$\boldsymbol{Q}_n \equiv \begin{bmatrix} \text{Re}[H_{1n}] & \text{Im}[H_{1n}] & \text{Re}[H_{2n}] & \text{Im}[H_{2n}] \end{bmatrix}, \quad (5)$$

$$\boldsymbol{A} \equiv \begin{bmatrix} \text{Re}[A_1] & \text{Im}[A_1] & \text{Re}[A_2] & \text{Im}[A_2] \end{bmatrix}^{\text{T}}, \quad (6)$$

where

$$H_{kn} \equiv \iint_{\text{PD}_n} a_k^* b_k dxdy \quad (k = 1, 2). \quad (7)$$

To eliminate the signal-signal beat component term that are non-linear with respect to $\boldsymbol{A}$, differential photodetection is generally required. This operation is mathematically written as

$$\boldsymbol{S} = \mathbf{C}\boldsymbol{I}, \quad (8)$$

where $\boldsymbol{S}$ denotes the four real-valued signal components, $\mathbf{C}$ is a $4 \times N$ matrix representing the differentiation operation, and $\boldsymbol{I} \equiv [I_1, \ldots, I_N]^{\text{T}}$. In order to remove the signal-signal beat

components, $\mathbf{C}$ must satisfy the following conditions:

$$\mathbf{C} \begin{bmatrix} P_{a11} \\ \vdots \\ P_{a1N} \end{bmatrix} = \mathbf{C} \begin{bmatrix} P_{a21} \\ \vdots \\ P_{a2N} \end{bmatrix} = \mathbf{0}. \quad (9)$$

When these conditions are satisfied, $\boldsymbol{S}$ is expressed by inserting (2) to (8) as

$$\boldsymbol{S} = R(\mathbf{CQ}\boldsymbol{A} + \boldsymbol{P}_{\Delta\text{LO}}), \quad (10)$$

where we define

$$\mathbf{Q} \equiv \begin{bmatrix} \boldsymbol{Q}_1 \\ \vdots \\ \boldsymbol{Q}_N \end{bmatrix}, \quad (11)$$

$$\boldsymbol{P}_{\Delta\text{LO}} \equiv \frac{1}{2}\mathbf{C} \begin{bmatrix} P_{b1} & \cdots & P_{bn} \end{bmatrix}^{\text{T}}. \quad (12)$$

In (10), the first term inside the parenthesis represents the signal-LO beat components, whereas the second term is a constant vector representing the remaining LO-LO beat components after the differentiation. If the matrix $\mathbf{CQ}$ is regular, the desired signal component $\boldsymbol{A}$ can be obtained from (10) as

$$\boldsymbol{A} = \frac{1}{R}(\mathbf{CQ})^{-1}(\boldsymbol{S} - R\boldsymbol{P}_{\Delta\text{LO}}). \quad (13)$$

B. Sensitivity Analysis

In general, the receiver sensitivity of a coherent receiver is ultimately limited by the shot noise. We consider a case where the detected PD current $\boldsymbol{I}_{\text{meas}}$ includes noise components $\boldsymbol{\Delta I} \equiv [\Delta I_1, \ldots, \Delta I_n]^{\text{T}}$ and is written as

$$\boldsymbol{I}_{\text{meas}} = \boldsymbol{I} + \boldsymbol{\Delta I}. \quad (14)$$

Assuming that LO light intensity is large compared with the signal, variance of the shot noise current can be expressed as [22]

$$\langle \Delta I_n^2 \rangle = 2qWI_n \approx qWRP_{bn}, \quad (15)$$

where q is the elementary charge and W is the detection bandwidth. We can calculate the variance of the difference between the decoded IQ signal $\widetilde{\boldsymbol{A}}$ retrieved from $\boldsymbol{I}_{\text{meas}}$ and the actual IQ signal $\boldsymbol{A}$ (see Appendix A for details) as

$$\varepsilon \equiv \langle \|\widetilde{\boldsymbol{A}} - \boldsymbol{A}\|^2 \rangle = \frac{qW}{R} \|(\mathbf{CQ})^{-1}\mathbf{C}\boldsymbol{\Sigma}_L\|_F^2, \quad (16)$$

where $\boldsymbol{\Sigma}_L$ is a $N \times N$ diagonal matrix consisting of the square roots of the LO light intensity expressed as

$$\boldsymbol{\Sigma}_L \equiv \begin{bmatrix} \sqrt{P_{b1}} & & \\ & \ddots & \\ & & \sqrt{P_{bN}} \end{bmatrix}. \quad (17)$$

We now define a dimensionless parameter K as

$$K \equiv \frac{R\varepsilon}{qW} = \|(\mathbf{CQ})^{-1}\mathbf{C}\boldsymbol{\Sigma}_L\|_F^2. \quad (18)$$

Since K is proportional to the normalized noise ε, it is useful in comparing the receiver sensitivity of different configurations.

In the following, we evaluate the quantitative receiver sensitivity assuming that the incident signal power is normalized, so that $\iint |a_1|^2 dxdy = \iint |a_2|^2 dxdy = 1$, and the LO power is sufficiently large so that $\iint \|\boldsymbol{E}_{\mathrm{LO}}\|^2 dxdy = P_{\mathrm{LO}} \gg 1$.

First, we consider a conventional DP coherent receiver with a $90°$ hybrid ($N = 8$) under ideal conditions. We assume that the x- and y-polarization components of the signal and LO light are split and focused to $n = 1, \ldots, 4$ and $n = 5, \ldots, 8$, respectively, with equal power and precise phase relationship. Then, the signal and LO power detected by each PD can be expressed as

$$P_{bn} = \frac{P_{\mathrm{LO}}}{8},$$

$$P_{a1n} = \begin{cases} \frac{1}{4} & (n = 1, \ldots, 4) \\ 0 & (n = 5, \ldots, 8) \end{cases},$$

$$P_{a2n} = \begin{cases} 0 & (n = 1, \ldots, 4) \\ \frac{1}{4} & (n = 5, \ldots, 8) \end{cases}. \quad (19)$$

Considering the phase shift of $90°$ hybrid, H_{kn} and $\mathbf{Q}$ are written as

$$\begin{bmatrix} H_{11} & \cdots & H_{18} \end{bmatrix}$$
$$= |H| \begin{bmatrix} 1 & -1 & i & -i & 0 & 0 & 0 & 0 \end{bmatrix}, \quad (20)$$

$$\begin{bmatrix} H_{21} & \cdots & H_{28} \end{bmatrix} = |H| \begin{bmatrix} 0 & 0 & 0 & 0 & 1 & -1 & i & -i \end{bmatrix}, \quad (21)$$

$$\mathbf{Q} = |H| \begin{bmatrix} 1 & 0 & 0 & 0 \\ -1 & 0 & 0 & 0 \\ 0 & 1 & 0 & 0 \\ 0 & -1 & 0 & 0 \\ 0 & 0 & 1 & 0 \\ 0 & 0 & -1 & 0 \\ 0 & 0 & 0 & 1 \\ 0 & 0 & 0 & -1 \end{bmatrix}, \quad (22)$$

where $|H|$ is defined as

$$|H_{kn}| = \sqrt{P_{akn}P_{bn}} = \frac{\sqrt{P_{\mathrm{LO}}}}{4\sqrt{2}} \equiv |H|. \quad (23)$$

The matrix $\mathbf{C}$ for the four balanced PDs is expressed as

$$\mathbf{C} = \begin{bmatrix} 1 & -1 & 0 & 0 & 0 & 0 & 0 & 0 \\ 0 & 0 & 1 & -1 & 0 & 0 & 0 & 0 \\ 0 & 0 & 0 & 0 & 1 & -1 & 0 & 0 \\ 0 & 0 & 0 & 0 & 0 & 0 & 1 & -1 \end{bmatrix}. \quad (24)$$

By inserting parameters of (19), (22), and (24) to (18), we obtain

$$K = 8. \quad (25)$$

Next, we investigate the sensitivity of our proposed configuration with five PDs ($N = 5$) shown in Fig. 1. Assuming that the power transmittance of the beam splitter (BS) is T, signal and LO power at each PD can be written as

$$P_{bn} = \frac{1-T}{5} P_{\mathrm{LO}}, \quad P_{a1n} = P_{a2n} = \frac{T}{5} \quad (26)$$

Since half of the LO power interferes with each polarization of the signal in this case, $|H_{kn}|$ can be written as

$$|H_{kn}| = \sqrt{\frac{1}{2} P_{akn}P_{bn}} = \frac{\sqrt{T(1-T)P_{\mathrm{LO}}}}{5\sqrt{2}} \equiv |H|. \quad (27)$$

Then, H_{kn} and $\mathbf{Q}$ are derived as

$$\begin{bmatrix} H_{11} & \cdots & H_{15} \end{bmatrix}$$
$$= |H| \begin{bmatrix} 1 & e^{i2\pi/5} & e^{i4\pi/5} & e^{-i4\pi/5} & e^{-i2\pi/5} \end{bmatrix}, \quad (28)$$

$$\begin{bmatrix} H_{21} & \cdots & H_{25} \end{bmatrix}$$
$$= |H| \begin{bmatrix} 1 & e^{i4\pi/5} & e^{-i2\pi/5} & e^{i2\pi/5} & e^{-i4\pi/5} \end{bmatrix}, \quad (29)$$

$$\mathbf{Q} = |H| \begin{bmatrix} 1 & 0 & 1 & 0 \\ \cos\frac{2\pi}{5} & \sin\frac{2\pi}{5} & \cos\frac{4\pi}{5} & \sin\frac{4\pi}{5} \\ \cos\frac{4\pi}{5} & \sin\frac{4\pi}{5} & \cos\frac{-2\pi}{5} & \sin\frac{-2\pi}{5} \\ \cos\frac{-4\pi}{5} & \sin\frac{-4\pi}{5} & \cos\frac{2\pi}{5} & \sin\frac{2\pi}{5} \\ \cos\frac{-2\pi}{5} & \sin\frac{-2\pi}{5} & \cos\frac{-4\pi}{5} & \sin\frac{-4\pi}{5} \end{bmatrix} \quad (30)$$

Since we take the difference between the photocurrents of adjacent PDs, $\mathbf{C}$ is written as

$$\mathbf{C} = \begin{bmatrix} 1 & -1 & 0 & 0 & 0 \\ 0 & 1 & -1 & 0 & 0 \\ 0 & 0 & 1 & -1 & 0 \\ 0 & 0 & 0 & 1 & -1 \end{bmatrix}. \quad (31)$$

Note that the LO-LO beat component is also eliminated by the current differentiation in this case, leading to $\boldsymbol{P}_{\Delta\mathrm{LO}} = 0$. Inserting (26), (30), and (31) to (18), we obtain

$$K = \frac{16}{T}. \quad (32)$$

From (32), we see that K approaches 16 by increasing T, provided that sufficient LO power is input to the receiver. Consequently, we can conclude that the theoretical sensitivity limit of the proposed configuration is half of the conventional polarization-diversity $90°$-hybrid configuration given by (25). This 3-dB penalty originates from the fact that both polarization components of the signal are mixed with the LO light and received together in our five-PD scheme. This is in contrast to the conventional polarization-diversity configuration with eight PDs, where orthogonal polarization components of the signal are first demultiplexed, then combined with the LO light having the same polarization state, and finally detected by separate PDs for respective polarizations. In the proposed method, therefore, only half of the detected signal in average has the same polarization state as the LO light and can interfere to generate the signal-LO beat components, resulting in a 3-dB penalty.

Although the theoretical 3-dB reduction in the sensitivity is obviously a drawback of our five-PD configuration, we should note that fiber-to-chip coupling losses at GCs and insertion losses at the waveguide-based $90°$ optical hybrids, which are required in conventional DP coherent receivers, can easily add up to exceed 3 dB in practice [23], [24]. These losses should be eliminated or relaxed in our surface-normal receiver. In addition,
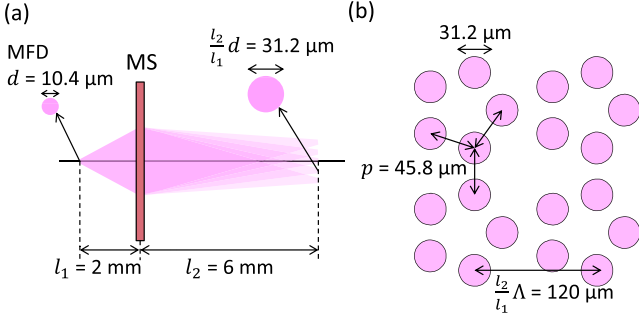
Fig. 2. Functionalities of the designed MS. (a) Light propagation from each core. MFD: mode field diameter. (b) Intensity pattern on the PD array surface when a four-core MCF ($\Lambda = 40$ μm) is placed at the input. The light from each core forms a regular pentagon.

the elimination of PBS and reduction of the number of PDs from eight to five in our scheme would offer a substantial advantage in minimizing the device footprint and complexity. Besides, in a system where an optical preamplifier is deployed before the receiver, the amplified-spontaneous-emission (ASE) noise becomes dominant. In such a case, the proposed scheme does not have any sensitivity penalty compared with conventional polarization-diversity-based DP coherent receivers.

Finally, we should note that the minimum number of PDs to demodulate a DP coherent signal by linear operations in general is five. Through a numerical parameter search, it is confirmed that our proposed scheme with the phase distributions shown in Fig. 1(b) exhibits the theoretical maximum sensitivity among all the possible phase configurations using five PDs.

III. DESIGN AND FABRICATION OF METASURFACE

To experimentally demonstrate the proposed device, we designed and fabricated an MS composed of Si nanoposts on SiO_2. The MS was designed to focus light from each core into five different spots with precise phase relationship as derived in the previous section. Fig. 2 illustrates the setup, where a fiber output is placed at a distance of l_1 from the MS and focused at a distance of l_2 from the MS output. Assuming an input fiber with the mode field diameter (MFD) of d, the diameter of each focused spot would be $(l_2/l_1)d$. Then, when an MCF with the core spacing of Λ is deployed, convolutions of these five spots would appear at the focal plane with a distance of $(l_2/l_1)\Lambda$.

In this work, a four-core step-index MCF [25] with $d = 10.4$ μm and $\Lambda = 40$ μm at a wavelength of 1550 nm was employed. The diameter of the focused spot was set to 31.2 μm by setting $l_1 = 2$ mm and $l_2 = 6$ mm. The diameter of entire MS region was set to 600 μm, so that more than 99% of the light emitted from the fiber was captured. To simplify the design of MS, a highly symmetric structure is preferable. Thus, the focal points were arranged in a regular pentagon, as depicted in Fig. 2(b). The size of the regular pentagon was determined to maximize the spacing between the focal points, resulting in a spacing of $p = 45.8$ μm. Assuming Gaussian beam approximation, we estimated that 98.7% of the total optical power of each
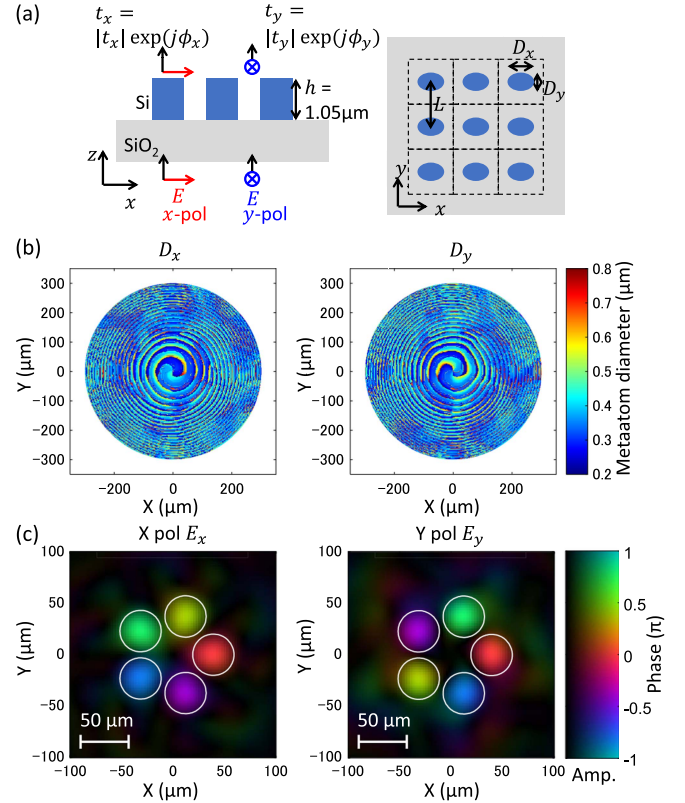

Fig. 3. Design and numerical analysis of MS. (a) Schematic of the MS composed of Si elliptical nanoposts on SiO_2, having the x and y diameters of (D_x, D_y) and the lattice constant of L. (b) Designed distributions of D_x and D_y for $L = 0.9$ μm. (c) Electric field distribution on the PD array obtained by FDTD simulation.

focused spot was within the diameter of p, indicating sufficiently low crosstalk to adjacent PDs.

The MS was designed based on the methodology demonstrated previously [26], [27]. As shown in Fig. 3(a), Si elliptical nanoposts with 1.05-μm height on a SiO_2 substrate were employed as meta-atoms and arranged in a square lattice. By adjusting the diameters (D_x, D_y) of each meta-atom, arbitrary phase shifts (ϕ_x, ϕ_y) for x- and y-polarization components could be applied. Using the rigorous coupled-wave analysis (RCWA), a look-up table (LUT) was first generated, which indicated the required (D_x, D_y) to achieve desired (ϕ_x, ϕ_y) [28]. Assuming the lattice constant L of 0.9 μm and the ranges of D_x and D_y from 200 nm to 840 nm, we successfully constructed LUT that gives arbitrary ϕ_x and ϕ_y with an average transmission as high as 94%.

The desired phase shift characteristics of MS were then calculated. The target phase profiles at the input and output of the MS were obtained through forward propagation from the input fiber mode as well as backward propagation from the ideal electric field at the PD array surface. By taking the difference of them, required phase profiles for x- and y-polarization components were obtained. Since dielectric MS can control only the phase, electric field profiles on the PD array generally deviate from the ideal ones, causing, for example, intensity variations between

each focal point. Nonetheless, owing to the high rotational symmetry in the complex amplitude distribution in the designed layout, such errors were minimized. Using these phase shift profiles and LUT, the distribution of meta-atom dimensions was derived as shown in Fig. 3(b).

To confirm the validity of the designed MS, rigorous simulation using the finite-difference time-domain (FDTD) method was performed. Fig. 3(c) shows the intensity and phase profiles of electric field (E_x, E_y) at the PD plane for x- and y-polarized inputs. The white line denotes the assumed photosensitive area of each PD, with a diameter of 40 μm. We can confirm that the light is focused at the five PDs with precise phase differences as designed. The total loss from incident light to PD is 3.1 dB and 3.7 dB for x and y polarizations, respectively. The intensity difference between different PDs is less than 0.2 dB, while the crosstalk from the neighboring input cores is suppressed below -16 dB for both polarization components. From (18), the receiver sensitivity penalty from the theoretical limit is derived to be 3.9 dB. Furthermore, it is numerically confirmed that the variation of sensitivity using our MS is less than 0.2 dB within the C-band, which is comparable or smaller than the loss variation of conventional waveguide-based 90° hybrids using multimode interference couplers [29].

The primary sources of the loss compared to the ideal case are attributed to two factors. First, since a lossless dielectric MS can only manipulate the optical phase, the actual wavefront generated by MS may not match perfectly with the ideal profile, which generally has a nonuniform intensity distribution. This difference is estimated to account for ~1 dB of loss. By employing dual MS configuration, it is possible to control both the intensity and phase distributions [30], which should reduce the penalty caused by such intensity mismatching. The second factor is the interaction between adjacent meta-atoms, which is estimated to contribute to ~2 dB of loss. While the LUT generated through RCWA assumes an infinite array of meta-atoms with identical dimensions, the actual designed MS consists of spatially varying meta-atoms, which results in phase errors. We can, therefore, expect that these losses can be eliminated to some extent by employing more sophisticated design algorithms that take into account complex interactions between neighboring meta-atoms [31], [32], [33].

The designed MS was fabricated using a silicon-on-quartz (SOQ) substrate with 1.05-μm-thick crystalline Si layer. The meta-atom patterns were formed by electron-beam lithography with ZEP520 A resist, followed by inductively coupled plasma reactive-ion etching (ICP-RIE) using SF_6 and C_4F_8 gases (Bosch process). Microscope and scanning-electron-microscope (SEM) images of the fabricated MS with a diameter of 600 μm are shown in Fig. 4. By optimizing fabrication conditions, the undesired scalloping effect on the sidewalls induced by the Bosch process [34] was minimized. Besides, high sidewall verticality exceeding 88° and good in-plane uniformity were obtained. To evaluate the yield of our MS, we fabricated 20 devices on different chips and confirmed that the deviation of meta-atom dimensions was generally within ±10 nm, indicating high yield and reproducibility of our fabrication process.
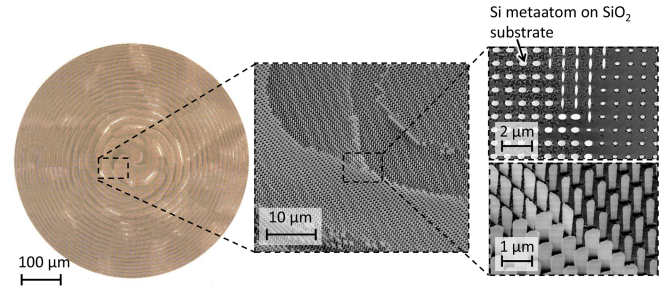

Fig. 4. Microscope and SEM images of the 600-μm-diameter MS fabricated on an SOQ substrate.

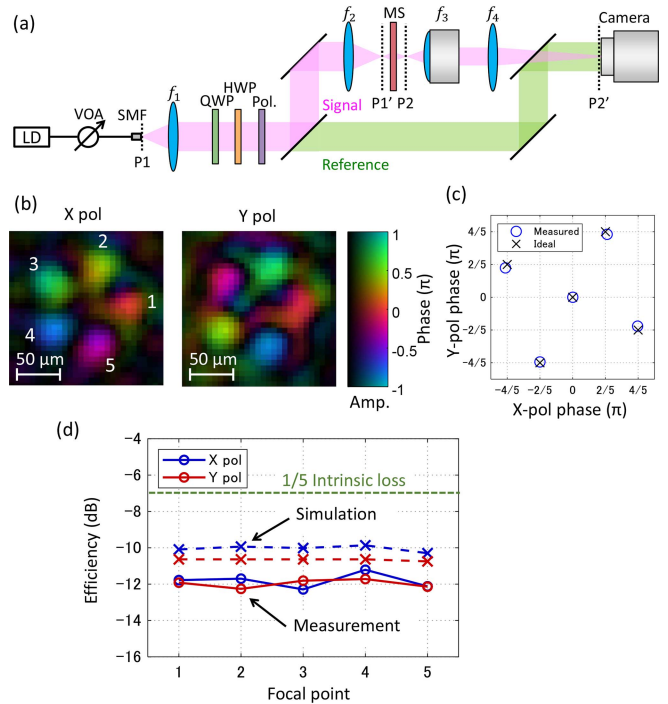

Fig. 5. Phase measurement of fabricated MS at 1550-nm wavelength for single-channel input. (a) Experimental setup. LD: laser diode, VOA: variable optical attenuator, SMF: single-mode fiber, QWP: quarter-wave plate, HWP: half-wave plate, Pol.: polarizer, $f_1 = f_2 = 50$ mm, $f_3 = 4$ mm, $f_4 = 200$ mm. (b) Electric field distribution at the PD array for x and y polarization inputs. (c) Relative optical phases of x and y components at each focal point. (d) Focusing efficiency at each focal point. Solid lines: measurement, dashed lines: FDTD simulation.

IV. CHARACTERIZATION OF METASURFACE

The fabricated MS was evaluated by measuring the intensity and phase characteristics at the focal plane. Fig. 5(a) illustrates the experimental setup. Continuous-wave (CW) light at a wavelength of 1550 nm was emitted from an SMF, focused at P1' plane, and incident on MS. The polarization state was controlled using a quarter-wave plate (QWP), a half-wave plate (HWP), and a polarizer. The focal plane P2 at the output of MS was magnified using a 4-f system comprising two lenses, f_3 and f_4, and then observed with an InGaAs camera (Hamamatsu C10633-13, 320×256 pixels). In order to measure phase profiles, a reference
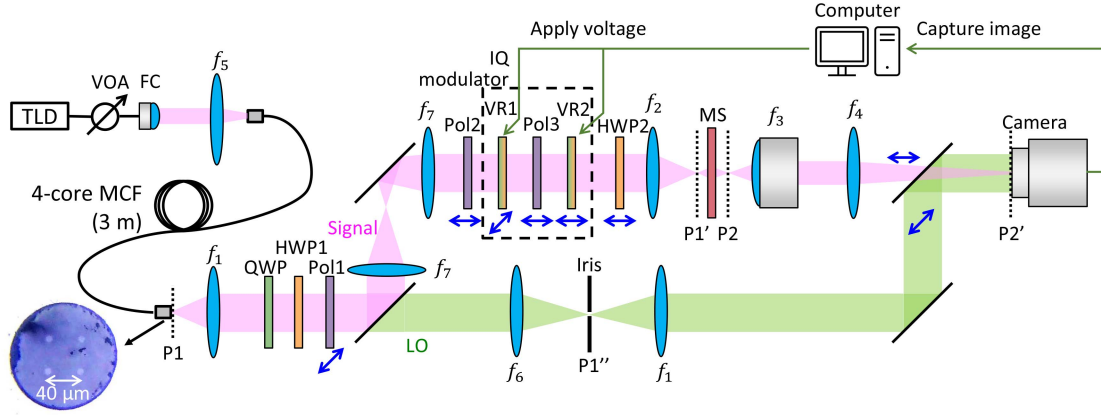
Fig. 6. Experimental setup of four-channel DP coherent detection using the fabricated MS and a step-index four-core MCF. TLD: tunable laser diode, FC: fiber collimator, VR: liquid-crystal-based variable retarder, $f_1 = f_2 = 50$ mm, $f_3 = 10$ mm, $f_4 = 200$ mm, $f_5 = 40$ mm, $f_6 = 125$ mm, $f_7 = 200$ mm. The components in the broken-line box are used to emulate an IQ modulator. Blue arrows indicate the angle of light polarization, the slow axes of the VRs, or the orientations of the polarizers.

path was placed by splitting the collimated beam and combined with the MS output to form an interferometer. We employed the digital off-axis holography method to extract phase information from the camera image [35], [36]. To measure the focusing efficiency, each focusing point was selected by an iris and the transmitted power was detected by an optical power meter.

Fig. 5(b) shows the complex amplitude distributions obtained for x- and y-polarization inputs. We can confirm that the light is focused precisely onto five points at the vertices of regular pentagon for both polarizations as designed. The optical phase at each focal point, averaged over the photosensitive area of each PD (indicated by white circles in Fig. 3(c)), is plotted for x- and y-polarization inputs in Fig. 5(c). The average and worst phase errors from the ideal case are 0.018π and 0.047π, respectively. Fig. 5(d) shows the measured focusing efficiencies to five points. The average efficiency to each of these five focal point is -11.8 dB (i.e., 4.8 dB below the intrinsic splitting loss of 1/5), so that the total insertion loss of our device is derived to be 4.8 dB. The intensity variations among the five focal points are less than 1.1 dB for both polarizations. The efficiencies obtained by the FDTD simulation are also plotted by the dashed lines for comparison. The $\sim$1.5-dB difference between the experiment and the simulations is attributed to imperfections in fabrication.

V. MULTI-CORE COHERENT DETECTION EXPERIMENT

Fig. 6 shows the experimental setup to demonstrate simultaneous homodyne detection of four-channel DP coherent signals from an MCF. CW light from a wavelength-tunable laser (Santec TSL-510) was irradiated to the input facet of a four-core step-index MCF (cladding diameter $= 125$ μm, MFD $= 10.4$ μm at $\lambda = 1550$ nm, $\Lambda = 40$ μm) through a focusing lens. Output light from MCF was converted to $45°$ linear polarization and split into two paths. One path (the lower path in Fig. 6) was used as a reference light or LO; we extracted the light from only one core by using an iris and collimated to an InGaAs camera. The other path (the upper path in Fig. 6) was used as a signal. As
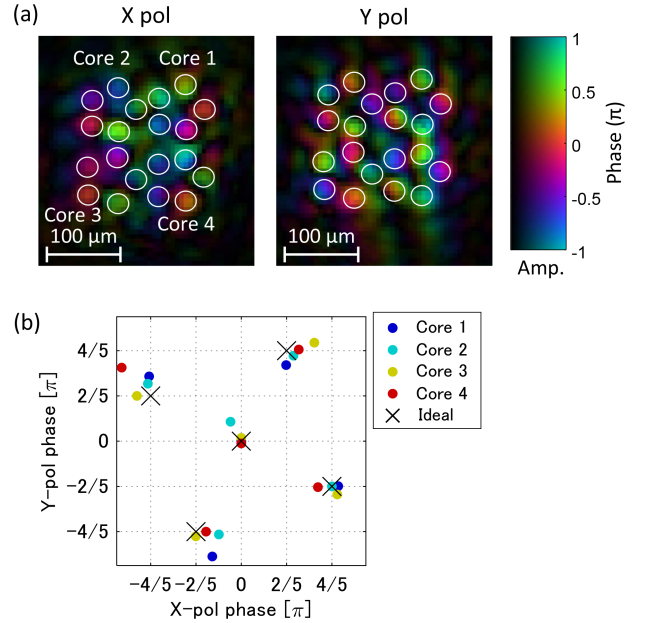

Fig. 7. Phase measurement of MS for four-core inputs at 1550-nm wavelength. (a) Electric field distribution at the PD array for x and y polarization inputs. (b) Relative optical phases of x and y components at each focal point for four cores.

shown by the broken-line box in Fig. 6, two liquid-crystal-based variable retarders (VRs) and a polarizer were used to emulate an IQ modulator. The IQ modulator was driven by a pseudorandom bit sequence (PRBS) mapped to 64-ary quadrature amplitude modulation (64QAM) format. The modulated signal was transmitted through MS after the incident polarization was controlled by HWP. Then, the output from MS was combined with LO and observed by a camera to acquire 4 cores $\times$ 5 points = 20 beat signals. Once again, we assumed that 20 PDs with diameters of 40 μm are placed at the white circles shown in Fig. 7(a). The modulation symbol was switched at approximately 1-second intervals (1 Bd), and camera images were acquired after VRs
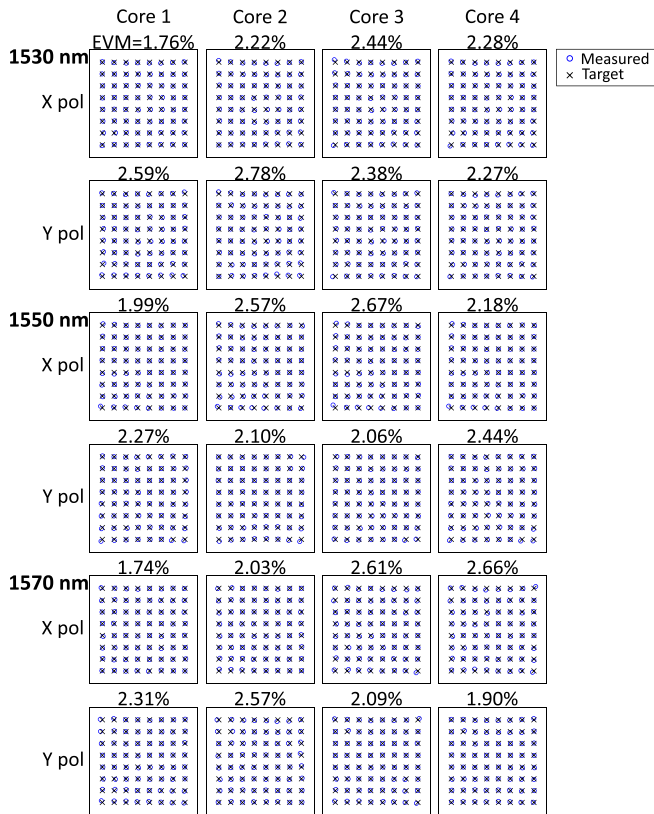
Fig. 8. Detection demonstration of four-core DP coherent receiver. Retrieved constellations of 64QAM signals at wavelengths of 1530, 1550, and 1570 nm. EVM: error vector magnitude.

Fig. 9. Measured wavelength dependence of EVM in C-band, derived from measured data in Fig. 8.

high-accuracy homodyne detection is achieved across the entire C-band.

VI. CONCLUSION

We have proposed and experimentally demonstrated a spatially scalable multi-core DP coherent receiver based on a dielectric MS. The proposed receiver realizes all the necessary functionalities of optical hybrids and focusing lenses for multiple channels using a single dielectric MS. Rigorous analytical model was introduced to derive explicit conditions for MS to achieve the highest receiver sensitivity. We designed and fabricated MS composed of Si nanoposts array on SiO_2 to demonstrate simultaneous detection of four DP 64QAM signals from a four-core step-index MCF. The EVM was less than 3% for all spatial/polarization channels from 1530 to 1570 nm. While the speed was limited by the InGaAs camera in this work, use of high-speed PD arrays [39], [40], [41] can easily achieve >100 Gb/s bandwidth per single spatial/polarization channel, enabling >Tb/s total data rate for four-core DP coherent signals. Our designed MS can simply replace micro-optic lenses used in conventional receivers and can be inserted between an MCF and a PD array separated by less than 1 cm. The entire receiver can therefore be assembled into a compact module equivalent to current commercial single-channel coherent receivers [42], enabling low-cost and practical SDM coherent receivers without PBS and FIFO devices.

Finally, we should note that the scalable coherent receiver demonstrated in this work would be useful not only in optical communications and interconnects, but also in various other emerging applications. For example, frequency-modulated continuous-wave (FMCW) light detection and ranging (LiDAR) systems utilize the coherent nature of lightwaves to achieve high-sensitivity three-dimensional (3D) sensing. Compact and large-scale coherent receiver arrays are desired to achieve high-speed and high-resolution 3D imaging without using bulky and fragile mechanical beam steerers [43]. In the field of optical neural networks, on the other hand, scalable coherent receiver arrays would be useful in performing large-scale multiply–accumulate operations in the optical domain at ultra-low latency and computational energy [44], [45]. We, therefore, believe that this work paves the way for a wide range of applications that

were stabilized. Note that the modulation speed was limited by the read-out time of the camera and the response time of VRs in this experiment. A real-valued 5×2 MIMO adaptive equalizer by a decision-driven least-mean-square (DD-LMS) algorithm [37], [38] was applied to obtain IQ components and to compensate for any polarization variation inside MCF and other fluctuations in the setup. Prior to the experiment, the adaptive equalizer was trained using transmitted symbols. Then, no knowledge about the transmitted data was used during the measurement to retrieve IQ signals.

First, complex optical field distributions on the focal plane of MS measured at 1550-nm wavelength without IQ modulation are shown in Fig. 7(a) for both polarizations. Once again, the relative optical phases are extracted from these distributions for 20 focal points and plotted in Fig. 7(b). Now, we see that the signals from the four cores are focused on 20 spots with the same relative optical phases as in the single-core case shown in Fig. 5(b). The average and worst phase errors compared with the ideal case for the 20 focusing spots are 0.074π and 0.26π, respectively. Finally, Fig. 8 shows the retrieved constellations of x- and y-polarization components from all four cores at wavelengths of 1530, 1550, and 1570 nm. Here, an averaged value of approximately 500 symbols is shown for each constellation. The error vector magnitude (EVM) derived from Fig. 8 is plotted for each wavelength in Fig. 9. The EVM is less than 3% for all wavelengths, cores, and polarization states, demonstrating that
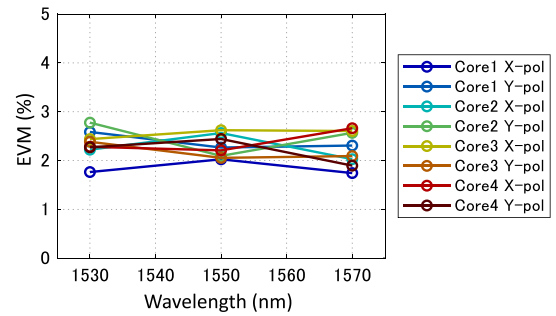
utilize the spatial parallelism of coherent light, including optical communication, sensing, and computing.

APPENDIX A
DERIVATION OF SENSITIVITY FORMULA

Based on (13) and (14), The difference between the received symbol $\widetilde{A}$ and the actual symbol A is expressed as

$$\widetilde{A} - A = \frac{1}{R}(\mathbf{CQ})^{-1}\mathbf{C}\boldsymbol{\Delta} I. \tag{33}$$

To quantitatively evaluate the sensitivity of receivers with different configurations, we derive the expression for the variance ε defined as

$$\varepsilon \equiv \langle\|\widetilde{A} - A\|^2\rangle = \frac{1}{R^2}\langle\|(\mathbf{CQ})^{-1}\mathbf{C}\boldsymbol{\Delta} I\|^2\rangle. \tag{34}$$

Since the shot noise expressed by (15) is superimposed on each PD current, the noise vector $\boldsymbol{\Delta} I$ follows an N-dimensional Gaussian distribution $\mathcal{N}_N$ as

$$\boldsymbol{\Delta} I \sim \mathcal{N}_N(\mathbf{0}, qWR\boldsymbol{\Sigma}_L\boldsymbol{\Sigma}_L^\dagger). \tag{35}$$

It is known that a general N-dimensional vector $\boldsymbol{X} \equiv [X_1, \ldots, X_N]^{\mathrm{T}} \sim \mathcal{N}_N(\boldsymbol{\mu}, \boldsymbol{\Sigma})$ has a following property about a transformation by a $N \times N$ matrix $\mathbf{M}$ [46]:

$$\mathbf{M}\boldsymbol{X} \sim \mathcal{N}_N(\mathbf{M}\boldsymbol{\mu},\ \mathbf{M}\boldsymbol{\Sigma}\mathbf{M}^\dagger). \tag{36}$$

Applying (35) and (36) to (33), the distribution of $\widetilde{A} - A$ can be written as

$$\widetilde{A} - A \sim \mathcal{N}_N\left(\mathbf{0},\ \frac{qW}{R}(\mathbf{CQ})^{-1}\mathbf{C}\boldsymbol{\Sigma}_L\boldsymbol{\Sigma}_L^\dagger\mathbf{C}^\dagger((\mathbf{CQ})^{-1})^\dagger\right). \tag{37}$$

Next, the variance of the norm of $\boldsymbol{X}$ is calculated as

$$\langle\|\boldsymbol{X}\|^2\rangle = \left\langle\sum_{n=1}^N X_n^2\right\rangle = \sum_{n=1}^N\langle X_n^2\rangle. \tag{38}$$

where X_n is the n-th element of $\boldsymbol{X}$, which follows the one-dimensional Gaussian distribution. When the mean and the standard deviation of X_n are defined as μ_n and σ_n, the second order moment $\langle X_n^2\rangle$ can be calculated using the moment generating function $M_{X_n}(t) = \exp(\mu_n t + \sigma_n^2 t^2/2)$ as

$$\langle X_n^2\rangle = \left.\frac{d^2 M_{X_n}}{dt^2}\right|_{t=0} = \mu_n^2 + \sigma_n^2. \tag{39}$$

Equations (38) and (39) yield

$$\langle\|\boldsymbol{X}\|^2\rangle = \sum_{n=1}^N(\mu_n^2 + \sigma_n^2) = \|\boldsymbol{\mu}\|^2 + \mathrm{tr}(\boldsymbol{\Sigma}). \tag{40}$$

Applying (37) and (40) to (34), ε is expressed as

$$\varepsilon = \frac{qW}{R}\mathrm{tr}[(\mathbf{CQ})^{-1}\mathbf{C}\boldsymbol{\Sigma}_L\boldsymbol{\Sigma}_L^\dagger\mathbf{C}^\dagger((\mathbf{CQ})^{-1})^\dagger]$$
$$= \frac{qW}{R}\|(\mathbf{CQ})^{-1}\mathbf{C}\boldsymbol{\Sigma}_L\|_F^2. \tag{41}$$

Here, we used the Frobenius norm defined as

$$\|\mathbf{M}\|_F \equiv \sqrt{\mathrm{tr}[\mathbf{MM}^\dagger]}. \tag{42}$$

REFERENCES

[1] P. J. Winzer and D. T. Neilson, "From scaling disparities to integrated parallelism: A decathlon for a decade," *J. Lightw. Technol.*, vol. 35, no. 5, pp. 1099–1115, Mar. 2017.

[2] P. J. Winzer, D. T. Neilson, and A. R. Chraplyvy, "Fiber-optic transmission and networking: The previous 20 and the next 20 years [invited]," *Opt. Exp.*, vol. 26, no. 18, pp. 24190–24239, Sep. 2018.

[3] X. Zhou, R. Urata, and H. Liu, "Beyond 1 Tb/s intra-data center interconnect technology: IM-DD or coherent?," *J. Lightw. Technol.*, vol. 38, no. 2, pp. 475–484, Feb. 2020.

[4] D. Tauber et al., "Role of coherent systems in the next DCI generation," *J. Lightw. Technol.*, vol. 41, no. 4, pp. 1139–1151, Feb. 2023.

[5] J. Zhang and Z. Jia, "Coherent passive optical networks for 100 G/λ-And-Beyond fiber access: Recent progress and outlook," *IEEE Netw.*, vol. 36, no. 2, pp. 116–123, Mar./Apr. 2022.

[6] D. J. Richardson, J. M. Fini, and L. E. Nelson, "Space-division multiplexing in optical fibres," *Nat. Photon.*, vol. 7, no. 5, pp. 354–362, May 2013.

[7] B. J. Puttnam, G. Rademacher, and R. S. Luís, "Space-division multiplexing for optical fiber communications," *Optica*, vol. 8, no. 9, pp. 1186–1201, Sep. 2021.

[8] B. Puttnam et al., "22.9 Pb/s data-rate by extreme space-wavelength multiplexing," in *Proc. Eur. Conf. Opt. Commun.*, 2023, Paper Th.C.2.1.

[9] T. Gonda et al., "Design of multicore fiber having upgradability from standard single-mode fibers and its application," *J. Lightw. Technol.*, vol. 37, no. 2, pp. 396–403, Jan. 2019.

[10] H. Takeshita et al., "Demonstration of uncoupled 4-core multicore fiber in submarine cable prototype with integrated multicore EDFA," *J. Lightw. Technol.*, vol. 41, no. 3, pp. 980–988, Feb. 2023.

[11] B. Quigley and M. Cantono, "Boosting subsea cables with multicore fiber technology," Google Cloud, 2023. [Online]. Available: https://cloud.google.com/blog/products/infrastructure/delivering-multi-core-fiber-technology-in-subsea-cables

[12] B. G. Lee et al., "End-to-end multicore multimode fiber optic link operating up to 120 Gb/s," *J. Lightw. Technol.*, vol. 30, no. 6, pp. 886–892, Mar. 2012.

[13] P. De Heyn et al., "Ultra-dense 16 Gb/s NRZ GeSi EAM-PD arrays coupled to multicore fiber for short-reach 896 Gb/s optical links," in *Proc. Opt. Fiber Commun. Conf.*, 2017, Paper Th1B.7.

[14] M. Ayata et al., "All-plasmonic IQ modulator with a 36 µm fiber-to-fiber pitch," *J. Lightw. Technol.*, vol. 37, no. 5, pp. 1492–1497, Mar. 2019.

[15] Y. Tong et al., "1.12-Tbit/s PAM-4 enabled by a silicon photonic transmitter bridged with a 7-channel MCF," *IEEE Photon. Technol. Lett.*, vol. 32, no. 16, pp. 987–990, Aug. 2020.

[16] C. R. Doerr et al., "Monolithic polarization and phase diversity coherent receiver in silicon," *J. Lightw. Technol.*, vol. 28, no. 4, pp. 520–525, Feb. 2010.

[17] A. Mekis et al., "A grating-coupler-enabled CMOS photonics platform," *IEEE J. Sel. Top. Quantum Electron.*, vol. 17, no. 3, pp. 597–608, May/Jun. 2011.

[18] C. R. Doerr and T. F. Taunay, "Silicon photonics core-, wavelength-, and polarization-diversity receiver," *IEEE Photon. Technol. Lett.*, vol. 23, no. 9, pp. 597–599, May 2011.

[19] K. Komatsu et al., "FIFO-free 4-core dual-polarization optical hybrid using a single dielectric metasurface," in *Proc. Eur. Conf. Opt. Commun.*, 2023, Paper Th.C.1.3.

[20] K. Komatsu, G. Soma, K. Mizukami, S. Ishimura, H. Takahashi, and M. Suzuki, "Surface-normal dual-polarization coherent receiver using dielectric metasurface," in *Proc. Conf. Lasers Electro-Opt.*, 2023, Paper SM4G.1.

[21] G. Soma et al., "Integrated dual-polarization coherent receiver without a polarization splitter-rotator," *Opt. Exp.*, vol. 29, no. 2, pp. 1711–1721, Jan. 2021.

[22] K. Kikuchi, "Fundamentals of coherent optical fiber communications," *J. Lightw. Technol.*, vol. 34, no. 1, pp. 157–179, Jan. 2016.

[23] P. Dong, X. Liu, S. Chandrasekhar, L. L. Buhl, R. Aroca, and Y.-K. Chen, "Monolithic silicon photonic integrated circuits for compact 100^+ gb/s coherent optical receivers and transmitters," *IEEE J. Sel. Top. Quantum Electron.*, vol. 20, no. 4, pp. 150–157, Jul./Aug. 2014 .

[24] H. Yagi et al., "InP-based p-i-n-photodiode array integrated with 90° hybrid using butt-joint regrowth for compact 100 gb/s coherent receiver," *IEEE J. Sel. Top. Quantum Electron.*, vol. 20, no. 6, Nov./Dec. 2014, Art. no. 3900107.

[25] T. Matsui, Y. Sagae, T. Sakamoto, and K. Nakajima, "Design and applicability of multi-core fibers with standard cladding diameter," *J. Lightw. Technol.*, vol. 38, no. 21, pp. 6065–6070, Nov. 2020.

[26] A. Arbabi, Y. Horie, M. Bagheri, and A. Faraon, "Dielectric metasurfaces for complete control of phase and polarization with subwavelength spatial resolution and high transmission," *Nat. Nanotechnol.*, vol. 10, no. 11, pp. 937–943, Nov. 2015.

[27] G. Soma, Y. Nomoto, T. Umezawa, Y. Yoshida, Y. Nakano, and T. Tanemura, "Compact and scalable polarimetric self-coherent receiver using a dielectric metasurface," *Optica*, vol. 10, no. 5, pp. 604–611, May 2023.

[28] V. Liu and S. Fan, "S^4: A free electromagnetic solver for layered periodic structures," *Comput. Phys. Commun.*, vol. 183, no. 10, pp. 2233–2244, May 2012.

[29] S. H. Jeong and K. Morito, "Novel optical 90° hybrid consisting of a paired interference based 2 MMI coupler, a phase shifter and a 2 MMI coupler," *J. Lightw. Technol.*, vol. 28, no. 9, pp. 1323–1331, 2010.

[30] J. Oh et al., "Metasurfaces for free-space coupling to multi-core fibers," *J. Lightw. Technol.*, early access, Nov. 21, 2023, doi: 10.1109/JLT.2023.3335334.

[31] L. Hsu, M. Dupré, A. Ndao, J. Yellowhair, and B. Kanté, "Local phase method for designing and optimizing metasurface devices," *Opt. Exp.*, vol. 25, no. 21, pp. 24974–24982, Oct. 2017.

[32] C. C. Nadell, B. Huang, J. M. Malof, and W. J. Padilla, "Deep learning for accelerated all-dielectric metasurface design," *Opt. Exp.*, vol. 27, no. 20, pp. 27523–27535, Sep. 2019.

[33] H. Yingli et al., "Physics-data-driven intelligent optimization for large-scale meta-devices," in *Proc. Opto-Electron. Adv.*, Nov. 2023, vol. 6, Art. no. 230133.

[34] B. Wu, A. Kumar, and S. Pamarthy, "High aspect ratio silicon etch: A review," *J. Appl. Phys.*, vol. 108, Sep. 2010, Art. no. 051101.

[35] E. Cuche, P. Marquet, and C. Depeursinge, "Spatial filtering for zero-order and twin-image elimination in digital off-axis holography," *Appl. Opt.*, vol. 39, no. 23, pp. 4070–4075, Jun. 2000.

[36] M. Zhao et al., "Phase characterisation of metalenses," *Light Sci. Appl.*, vol. 10, Mar. 2021, Art. no. 52.

[37] Y. Mori, C. Zhang, and K. Kikuchi, "Novel configuration of finite-impulse-response filters tolerant to carrier-phase fluctuations in digital coherent optical receivers for higher-order quadrature amplitude modulation signals," *Opt. Exp.*, vol. 20, no. 24, pp. 26236–26251, Nov. 2012.

[38] M. S. Faruk and K. Kikuchi, "Compensation for in-phase/quadrature imbalance in coherent-receiver front end for optical quadrature amplitude modulation," *IEEE photon. J.*, vol. 5, no. 2, Apr. 2013, Art. no. 7800110.

[39] T. Umezawa, T. Sakamoto, A. Kanno, N. Yamamoto, and T. Kawanishi, "High speed 2-D photodetector array for space and mode-division multiplexing fiber communications," *J. Lightw. Technol.*, vol. 36, no. 17, pp. 3684–3692, Sep. 2018.

[40] T. Umezawa, A. Matsumoto, K. Akahane, A. Kanno, and N. Yamamoto, "400-pixel high-speed photodetector for high optical alignment robustness FSO receiver," in *Proc. Opt. Fiber Commun. Conf.*, Mar. 2022, Paper M4I.3.

[41] G. Soma et al., "Ultra-broadband surface-normal coherent optical receiver with nanometallic polarizers," *ACS Photon.*, vol. 9, no. 8, pp. 2842–2849, Jul. 2022.

[42] OIF, "Implementation agreement for micro intradyne coherent receivers," OIF-DPC-MRX-02.0, Jun. 2017.

[43] C. Rogers et al., "A universal 3D imaging sensor on a silicon photonics platform," *Nature*, vol. 590, pp. 256–261, Feb. 2021.

[44] R. Hamerly, L. Bernstein, A. Sludds, M. Soljačić, and D. Englund, "Large-scale optical neural networks based on photoelectric multiplication," *Phys. Rev. X*, vol. 9, May 2019, Art. no. 021032.

[45] Z. Chen et al., "Coherent VCSEL homodyne neural networks," *Nat. Photon.*, vol. 17, no. 8, pp. 723–730, Aug. 2023.

[46] A. C. Rencher and W. F. Christensen, *Methods of Multivariate Analysis*. Hoboken, NJ, USA: Wiley, 2012.